

# Shape Control of Colloidal $\text{Cu}_{2-x}\text{S}$ Polyhedral Nanocrystals by Tuning the Nucleation Rates

Ward van der Stam,<sup>†</sup> Sabine Gradmann,<sup>‡</sup> Thomas Altantzis,<sup>§</sup> Xiaoxing Ke,<sup>§</sup> Marc Baldus,<sup>‡</sup> Sara Bals,<sup>§</sup> and Celso de Mello Donega<sup>\*,†</sup>

<sup>†</sup>Condensed Matter and Interfaces, Debye Institute for Nanomaterials Science, Utrecht University, P.O. Box 80000, 3508 TA Utrecht, The Netherlands

<sup>‡</sup>NMR Spectroscopy, Bijvoet Center for Biomolecular Research, Department of Chemistry, Faculty of Science, Utrecht University, Padualaan 8, 3584 CH Utrecht, The Netherlands

<sup>§</sup>EMAT, University of Antwerp, Groenenborgerlaan 171, B-2020 Antwerp, Belgium

## Supporting Information

**ABSTRACT:** Synthesis protocols for colloidal nanocrystals (NCs) with narrow size and shape distributions are of particular interest for the successful implementation of these nanocrystals into devices. Moreover, the preparation of NCs with well-defined crystal phases is of key importance. In this work, we show that Sn(IV)-thiolate complexes formed in situ strongly influence the nucleation and growth rates of colloidal  $\text{Cu}_{2-x}\text{S}$  polyhedral NCs, thereby dictating their final size, shape, and crystal structure. This allowed us to successfully synthesize hexagonal bifrustums and hexagonal bipyramid NCs with low-chalcocite crystal structure, and hexagonal nanoplatelets with various thicknesses and aspect ratios with the djurleite crystal structure, by solely varying the concentration of Sn(IV)-additives (namely,  $\text{SnBr}_4$ ) in the reaction medium. Solution and solid-state  $^{119}\text{Sn}$  NMR measurements show that  $\text{SnBr}_4$  is converted in situ to Sn(IV)-thiolate complexes, which increase the  $\text{Cu}_{2-x}\text{S}$  nucleation barrier without affecting the precursor conversion rates. This influences both the nucleation and growth rates in a concentration-dependent fashion and leads to a better separation between nucleation and growth. Our approach of tuning the nucleation and growth rates with in situ-generated Sn-thiolate complexes might have a more general impact due to the availability of various metal-thiolate complexes, possibly resulting in polyhedral NCs of a wide variety of metal-sulfide compositions.



## INTRODUCTION

In recent years, the scientific community has achieved a high level of mastery over the size, shape, and composition of colloidal nanocrystals (NCs) and heteronanocrystals (HNCs) of Cd- and Pb-chalcogenide compositions.<sup>1–4</sup> However, their further deployment into applications has been hindered by toxicity concerns.<sup>5–8</sup> The properties of copper chalcogenides ( $\text{Cu}_{2-x}\text{A}$  with A = S, Se and Te) make them attractive alternatives for Cd- and Pb-based semiconductors for several applications.<sup>6,8–10</sup> For instance,  $\text{Cu}_{2-x}\text{S}$  is a direct p-type semiconductor with a band gap that depends on its stoichiometry (1.1–1.4 eV for  $x = 0–0.04$ ; 1.5 eV for  $x = 0.2$ ; 2.0 eV for  $x = 1$ ).<sup>11–13</sup> The combination of a suitable band gap, high absorption coefficient ( $10^4 \text{ cm}^{-1}$ ), low cost, and low toxicity has made  $\text{Cu}_{2-x}\text{S}$  a promising candidate for large scale and sustainable implementation into photovoltaic (PV) devices.<sup>14,15</sup> Moreover,  $\text{Cu}_{2-x}\text{A}$  NCs can hold both excitons and tunable localized surface plasmon resonances on demand.<sup>9,13,16–18</sup> This makes  $\text{Cu}_{2-x}\text{A}$  NCs promising materials for photovoltaics,<sup>15</sup> photocatalysis,<sup>19</sup> sensing,<sup>20</sup> and nanoplasmonics.<sup>9,11,17,21,22</sup>

The application of colloidal NCs in photovoltaic and nanoplasmonic devices requires strict control over the size, shape, and polydispersity of the NC ensemble because these

characteristics are of crucial importance not only for the optoelectronic properties of the NCs themselves but also for the quality of the NC thin films obtained by solution-based deposition techniques.<sup>23–25</sup>  $\text{Cu}_{2-x}\text{S}$  NCs are of particular interest because a variety of shapes not attainable for other semiconductor NCs can easily be synthesized with narrow size and shape distributions. For example, hexagonal nanodisks, nanoplatelets, and nanosheets, among other polyhedral shapes, have been successfully synthesized.<sup>6,26–29</sup> Shape control over  $\text{Cu}_{2-x}\text{S}$  NCs may also have a more general impact because  $\text{Cu}^+$  ions in copper chalcogenides have been shown to be easily exchangeable by other cations.<sup>6,30–37</sup> This opens up the possibility of using (partial) topotactic cation exchange reactions to convert  $\text{Cu}_{2-x}\text{A}$  NCs into other compositions while preserving the size and shape of the parent NCs, thereby making NCs with novel functionalities.<sup>33,36,37</sup> However, the methods currently available to control the size and shape of  $\text{Cu}_{2-x}\text{S}$  NCs lack flexibility because different sets of physical-chemical parameters (concentrations, ligands, reaction temperatures, reaction times) have to be used for each different

Received: July 27, 2016

Revised: August 30, 2016

Published: September 2, 2016

shape.<sup>6,26,28</sup> In this work, a novel methodology for the size and shape control of colloidal  $\text{Cu}_{2-x}\text{S}$  NCs is developed, which relies on changing just one single reaction variable: the concentration of Sn(IV) complexes that are used to control the nucleation and growth rates of  $\text{Cu}_{2-x}\text{S}$  NCs. In this way, hexagonal bifrustums, hexagonal bipyramids, and hexagonal nanoplatelets of various aspect ratios are synthesized with narrow size and shape distributions. Solid-state  $^{119}\text{Sn}$  NMR measurements indicate that Sn–thiolate complexes formed in situ control the nucleation and growth rates, which results in various polyhedral  $\text{Cu}_{2-x}\text{S}$  NCs. Our study provides insights into the formation of polyhedral  $\text{Cu}_{2-x}\text{S}$  NCs and possibly paves the way toward the development of synthetic protocols for polyhedral NCs of various compositions by deployment of in situ nucleation and growth controlling agents, such as Sn(IV)–thiolates.

## ■ EXPERIMENTAL SECTION

**Colloidal Hexagonal Bipyramid-Shaped  $\text{Cu}_{2-x}\text{S}$  NCs.** These NCs were synthesized based on the protocol described by Kuzuya et al.,<sup>38</sup> which was modified by adding  $\text{SnBr}_4$  to the reaction mixture. In a typical synthesis, 1.0 mmol  $\text{CuCl}$  (99 mg) and 0.5 mmol  $\text{SnBr}_4$  (219 mg) were mixed in 8 mL (33.6 mmol) of 1-dodecanethiol (DDT) and 2 mL (6 mmol) of oleylamine (OLAM). The flask was purged with  $\text{N}_2$ , and the solution was gradually heated to 225 °C. At first, a creamy white substance was present, but around 80 °C, the solution turned slightly yellow. When further heated, a clear yellow solution was obtained around 130 °C. Nucleation and growth of  $\text{Cu}_{2-x}\text{S}$  started when the temperature reached 200 °C. Finally, the particles were allowed to grow at 225 °C for 1 h, and subsequently, the nanoparticles were precipitated by the repeated addition of a methanol/butanol solution and redispersion in toluene.

**Colloidal Polyhedral  $\text{Cu}_{2-x}\text{S}$  NCs of Various Morphologies.** These NCs were synthesized based on the same method as described above only with the amount of  $\text{SnBr}_4$  varied (Cu:Sn ratio of 2:3 for low aspect ratio hexagonal nanoplatelets, 1:2 for high aspect ratio hexagonal nanoplatelets, 30:1 for small hexagonal bifrustums, and 1:1 for large hexagonal bipyramids).

**Transmission Electron Microscopy (TEM) and Energy Dispersive X-ray Spectroscopy (EDS).** TEM and EDS measurements were performed on a Tecnai20F (FEI) microscope equipped with a Field Emission Gun, a Gatan 694 CCD camera, and an EDAX spectrometer. The microscope was operated at 200 kV. Acquisition time for EDS measurements was 30 s. Samples for TEM imaging were prepared by dropping a diluted nanocrystal solution in toluene on a carbon-coated polymer film copper grid (300 mesh). The solvent (toluene) was allowed to evaporate prior to imaging.

**High-Resolution (Scanning) Transmission Electron Microscopy (HRTEM).** HRTEM measurements were performed on a double aberration-corrected cubed FEI Titan 50–80 electron microscope operated at 120 kV. HRTEM measurements were performed on FEI Osiris and FEI Tecnai electron microscopes operated at 200 kV. Electron tomography measurements were performed in high-angle annular dark-field scanning transmission electron microscopy (HAADF-STEM) mode to get rid of any unwanted diffraction contrast present in TEM by using an aberration-corrected cubed FEI Titan 60–300 electron microscope and a double aberration-corrected cubed FEI Titan 50–80 electron microscope operated at 200 and 300 kV. The acquisition of all of the series was performed manually over a tilt range from  $-74^\circ$  to  $+74^\circ$  and a tilt increment of  $2^\circ$  by using a Fischione model 2020 single tilt tomography holder. The alignment of all the acquired series was performed by using cross-correlation and the reconstruction by using the simultaneous iterative reconstruction technique (SIRT) as implemented in the ASTRA toolbox.<sup>39</sup>

**Solid-State  $^{119}\text{Sn}$  NMR and Solution  $^1\text{H}$  NMR.** These experiments were performed using a Bruker Avance III spectrometer equipped with a 4 mm double resonance probe head at 11.7 T static magnetic field. All experiments on precipitated and dry nanocrystals

were measured at room temperature and on solution samples at 308 K. Tin and proton field strengths for  $90^\circ$  pulses were 50 and 71 kHz, respectively. Spectral referencing was done using  $\text{SnBr}_4$  for tin and adamantane for protons. For solution  $^{119}\text{Sn}$  and  $^1\text{H}$  NMR measurements, no additional solvents were added. The crude reaction mixture was loaded in a capillary at elevated temperatures and subsequently cooled to room temperature before measurement. No precipitation was observed upon cooling.

**X-ray Diffraction (XRD).** XRD patterns were obtained using a PW 1729 Philips diffractometer equipped with a  $\text{Cu K}\alpha$  X-ray source ( $\lambda = 1.5418 \text{ \AA}$ ). Samples for XRD analysis were prepared by depositing purified NCs on a Si wafer substrate under an inert atmosphere. The purification procedure consisted of precipitating the NCs from a solution of NCs in toluene by adding anhydrous methanol (1:1 volume ratio). The sediment was isolated by centrifugation (3000 rpm, 15 min) and redispersed in chloroform. The concentrated solution of NCs was dropcasted on the Si wafer, and the chloroform was allowed to evaporate at RT, resulting in a concentrated NC solid.

**1D Powder Electron Diffraction (PED).** PED patterns were obtained by radially integrating the 2D ED patterns acquired on a Tecnai-12 transmission electron microscope using a selected-area aperture. 2D ED patterns were acquired on areas containing a large number of nanocrystals to make the 1D PED patterns statistically valid.

## ■ RESULTS AND DISCUSSION

**Shape Control of Anisotropic  $\text{Cu}_{2-x}\text{S}$  NCs by  $\text{SnBr}_4$  Addition.** Colloidal  $\text{Cu}_{2-x}\text{S}$  NCs were synthesized by heating a solution of  $\text{CuCl}$  in 1-dodecanethiol (DDT) and oleylamine (OLAM) to 225 °C. In this protocol, DDT has the combined roles of ligand, solvent, and sulfur source.<sup>38,40,41</sup> In the absence of  $\text{SnBr}_4$ , large polydisperse nanoplatelets ( $\sim 100 \text{ nm}$  lateral dimensions) are obtained (Figure 1a). The addition of  $\text{SnBr}_4$  to the reaction mixture has a dramatic impact on the size and shape of the product NCs, leading to a variety of polyhedral shapes (hexagonal bifrustums, hexagonal bipyramids, low and high aspect ratio hexagonal nanoplatelets) with small polydispersity, depending on the  $\text{SnBr}_4$  concentration (Figure 1).

High-resolution transmission electron microscopy (HRTEM) (Figure 2), electron diffraction (Figure S1), and X-ray diffractometry (Figure S2) measurements revealed that the product  $\text{Cu}_{2-x}\text{S}$  nanoplatelets have the djurleite crystal structure,<sup>42</sup> whereas the product  $\text{Cu}_{2-x}\text{S}$  bipyramids have the low-chalcocite crystal structure. This is evident in the HRTEM images and the corresponding fast fourier transform (FFT) patterns of hexagonal bipyramid NCs viewed along the [010] zone axis (Figure 2a,d and Figure S3) and of low aspect ratio nanoplatelets (Figure 2b,c,e,f). The observed spacings are in agreement (within a 1% error margin) with the djurleite crystal structure (lattice parameters  $a = 26.89 \text{ \AA}$ ,  $b = 15.74 \text{ \AA}$ , and  $c = 13.57 \text{ \AA}$ )<sup>42</sup> for the low aspect ratio nanoplatelets and with the low-chalcocite crystal structure (lattice parameters  $a = 11.92 \text{ \AA}$ ,  $b = 27.34 \text{ \AA}$ , and  $c = 13.44 \text{ \AA}$ )<sup>42</sup> for the bipyramid NCs. The high aspect ratio nanoplatelets also have the djurleite structure, whereas the hexagonal bifrustums have the low-chalcocite crystal structure (Figure S1).

The morphology of the NCs was investigated by carrying out electron tomography measurements in high-angle annular dark field scanning transmission electron microscopy (HAADF-STEM) mode (Figure 3). By combining the electron tomography results, which enabled the determination of the shape of the NCs, with the crystallographic information obtained by the HRTEM analysis (Figure 2 above), the different facets can be indexed according to the monoclinic low-

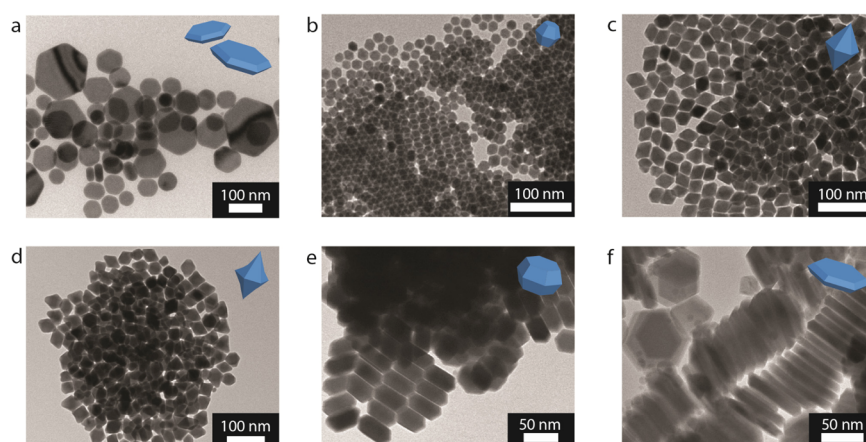


**Figure 1.** Representative transmission electron microscopy (TEM) images of  $\text{Cu}_{2-x}\text{S}$  nanocrystals synthesized with various  $\text{SnBr}_4$  concentrations under otherwise constant reaction conditions. The amount of  $\text{SnBr}_4$  was the only variable; all other reaction parameters were kept constant. (a) Polydisperse  $\text{Cu}_{2-x}\text{S}$  nanoplatelets synthesized in the absence of  $\text{SnBr}_4$ . (b) Monodisperse  $\text{Cu}_{2-x}\text{S}$  bifrustum NCs (diameter: 17 nm) are obtained when a small amount of  $\text{SnBr}_4$  is added (Cu:Sn 30:1). (c) A Cu:Sn ratio of 2:1 yields hexagonal bipyramids (28 nm wide, 38 nm long). (d)  $\text{Cu}_{2-x}\text{S}$  NCs synthesized under Cu:Sn = 1:1. (e) Hexagonal nanoplatelets (25 nm thick, 50 nm wide) are obtained under Cu:Sn = 2:3. (f) Further increasing the Cu:Sn ratio to 1:2 leads to wider and thinner hexagonal nanoplatelets (80 nm by 10 nm).

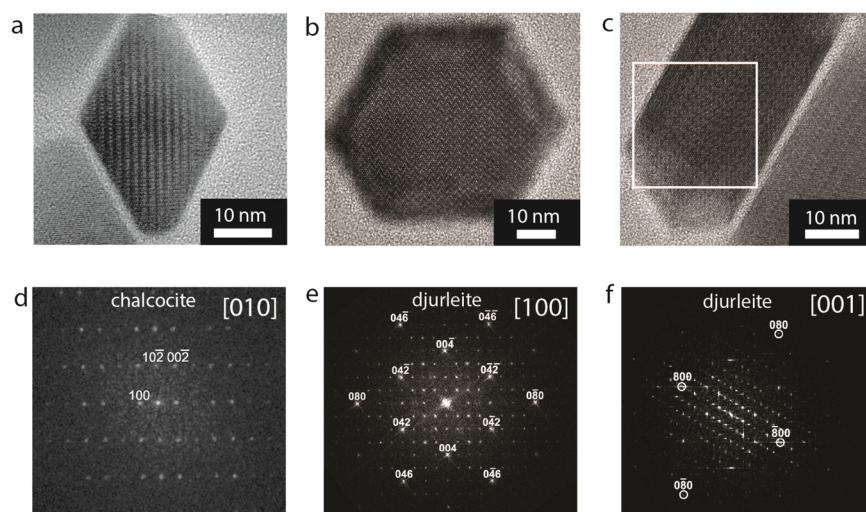


**Figure 2.** Structural analysis of the product  $\text{Cu}_{2-x}\text{S}$  nanocrystals. High-resolution transmission electron microscopy (HRTEM) images of (a) hexagonal bipyramid  $\text{Cu}_{2-x}\text{S}$  NCs and (b,c) low aspect ratio hexagonal  $\text{Cu}_{2-x}\text{S}$  nanoplatelets viewed along the [100] direction (b) and along the [001] direction (c). The white square in c indicates the area of which the FFT pattern is displayed in panel f. (d) FFT pattern of the bipyramid NC displayed in panel a, showing characteristic diffraction spots of the djurleite crystal structure viewed along the [010] zone axis. (e) FFT pattern of the NC displayed in panel b, showing characteristic diffraction spots of the djurleite crystal structure viewed along the [100] zone axis. (f) FFT pattern of a selected area (white square) of the NC displayed in panel c, showing characteristic diffraction spots of djurleite crystal structure viewed along the [001] direction.

chalcocite (for bipyramids) and monoclinic djurleite (for nanoplatelets) crystal structures.<sup>42</sup> In this way, the lateral facets of the low-chalcocite bipyramids are indexed as {364} (8 facets), {502} (2 facets), and {302} (2 facets) (Figure 3b,c). A different indexation holds for the low- and high aspect ratio hexagonal nanoplatelets, which have the djurleite crystal structure. The side facets of the nanoplatelets are formed by 8 trapezoidal {221} and 4 {101} facets, and the top and bottom facets are the hexagonal {100} facets. It is thus evident that the addition of  $\text{SnBr}_4$  alters the size and crystal structure, and hence, the faceting of  $\text{Cu}_{2-x}\text{S}$  NCs in a concentration-dependent fashion. At the lowest Cu:Sn ratio (30:1), small ( $d = 17$  nm) hexagonal bifrustums are obtained with the low-chalcocite crystal structure in which the top and bottom {102} facets and the {364} and {302}/ {502} side facets have similar

areas. Increasing the Cu:Sn ratio to 2:1 leads to large (28 nm by 38 nm), hexagonal bipyramidal low-chalcocite NCs in which the {102} facets are almost absent. Further increasing the Cu:Sn ratio results in djurleite hexagonal nanoplatelets of which the relative area of the {100} facets, the lateral dimensions, and the aspect ratio grow with the Cu:Sn ratio (25 nm thick and 50 nm wide for Cu:Sn = 2:3; 10 nm thick and 80 nm wide for Cu:Sn = 1:2). The formation mechanism for low-chalcocite bipyramids and djurleite nanoplatelets will be discussed in detail below.

Our group has previously reported that the addition of  $\text{SnBr}_4$  to synthesis protocols for  $\text{Cu}_{2-x}\text{S}$  NCs dramatically affects the size and shape of the product NCs, yielding ultrathin (2 nm thick)  $\text{Cu}_{2-x}\text{S}$  nanosheets with well-defined shape and size (triangular or hexagonal; 100 nm to 3  $\mu\text{m}$  wide) instead of

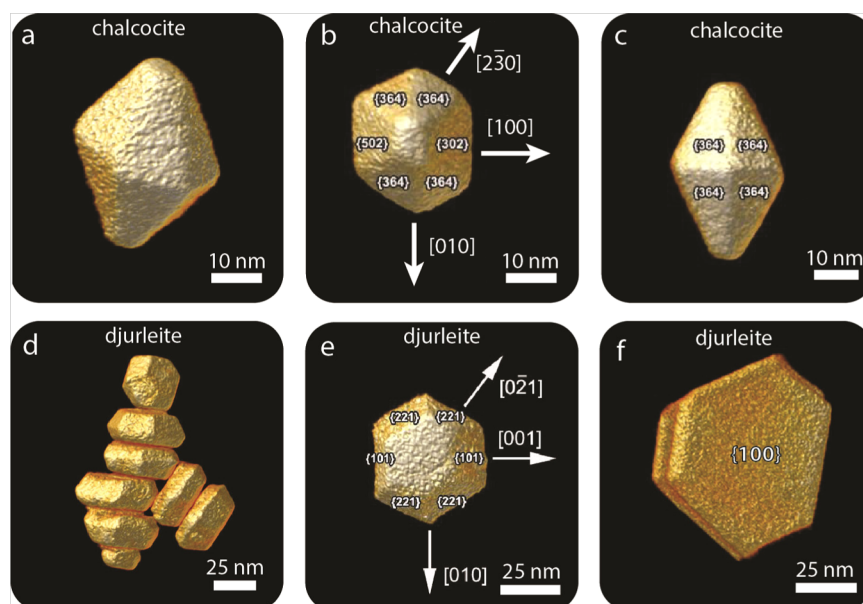


**Figure 3.** Electron tomography reconstructions of polyhedral  $\text{Cu}_{2-x}\text{S}$  nanocrystals. (a) Low-chalcocite hexagonal bipyramid nanocrystals. (b,c) Facet indexation of a low-chalcocite hexagonal bipyramid (b) viewed along the  $[001]$  direction and (c) along the  $[010]$  direction. (d) Djurleite low aspect ratio hexagonal nanoplatelets viewed along the  $[100]$  direction. (e) Facet indexation of a djurleite low aspect ratio hexagonal nanoplatelet viewed from the top. (f) Two high aspect ratio hexagonal nanoplatelets viewed from the top.

nearly spherical small (9 nm diameter) NCs.<sup>29,43</sup> The effect was clearly shown to be due to the halides, such that Sn(IV) tetrahalides were only relevant as sources of sufficiently high halide concentrations in the growth solution.<sup>29,43</sup> To investigate the roles of the halide and Sn(IV) in the present case, we carried out control experiments in which either  $\text{SnBr}_4$  was replaced by  $\text{Sn}(\text{OAc})_4$  or additional halides were added in the form of  $\text{CuBr}$  in the absence of any Sn(IV) compound. The results clearly show that, in contrast to our previous study on the formation of ultrathin  $\text{Cu}_{2-x}\text{S}$  nanosheets,<sup>29,43</sup> the effect in the present case is due to the Sn(IV) (Figure S4) because additional halides yield polydisperse nanoplatelets similar to those obtained under the standard reaction conditions (i.e.,  $\text{SnBr}_4$  absent; Figure 1a above), whereas addition of  $\text{Sn}(\text{OAc})_4$  resulted in polyhedral NCs similar to those obtained upon addition of  $\text{SnBr}_4$  ( $\text{Cu}:\text{Sn} = 2:1$ ; Figure 1c above). It should be noted that the polydispersity of the polyhedral NCs obtained by adding  $\text{Sn}(\text{OAc})_4$  is larger than that observed for the NCs formed in the presence of  $\text{SnBr}_4$ . This can be ascribed to the fact that  $\text{Sn}(\text{OAc})_4$  is less reactive toward DDT molecules than  $\text{SnBr}_4$  because acetate and  $\text{Sn}^{4+}$  are a strong Lewis base and acid, respectively, and are better matched in terms of hardness (both hard) than bromide and  $\text{Sn}^{4+}$  (soft and hard, respectively).<sup>44</sup> This suggests that the active Sn(IV) species responsible for the observed morphological changes results from a reaction between DDT and the added Sn(IV) salt. This also explains the different roles observed for Sn(IV) in the present work (active species) and in our previous study on the formation of  $\text{Cu}_{2-x}\text{S}$  nanosheets (namely, halide carrier)<sup>29,43</sup> because in the latter case a smaller excess of DDT (10-fold with respect to Cu and diluted in 1-octadecene) was injected in the reaction mixture, whereas in the present case, DDT is used as the solvent, resulting in a larger excess (30-fold with respect to Cu). This larger excess of DDT allows the formation of both Cu-DDT and Sn-DDT complexes, despite the lower reactivity of Sn(IV) toward DDT. As will become clear below in the NMR Spectroscopy section, another important chemical

difference in the present reaction system is the presence of oleylamine, which deprotonates DDT, thereby further facilitating its reaction with  $\text{SnBr}_4$ .

For gaining further insight into the role of  $\text{SnBr}_4$  in the shape control of the product  $\text{Cu}_{2-x}\text{S}$  NCs, energy dispersive X-ray spectroscopy (EDS) chemical mapping was used to quantify and locate the elements present in the NCs. The  $\text{Cu}:\text{Sn}:\text{S}$  ratio was found to be  $1.81 \pm 0.14:0.02 \pm 0.01:1.00$  regardless of the  $\text{Cu}:\text{Sn}$  ratio used in the reaction. Bromide was not detected in any sample. Elemental mapping shows that Sn is not homogeneously distributed across the ensemble of NCs but is concentrated on a few NCs that appear morphologically distinct from the majority of the ensemble (Figures S5 and S6). The Sn distribution in the Sn-poor NCs does not indicate any preference for a particular facet regardless of the shape of the NC (i.e., bipyramids or nanoplatelets in Figures S5 and S6, respectively). The signal from individual NCs was too low to allow the composition of the Sn-rich NCs to be reliably established, but their different shapes imply that they no longer have the djurleite or low-chalcocite crystal structures,<sup>42</sup> and may have adopted the cubic crystal structure characteristic of ternary  $\text{Cu}_x\text{Sn}_y\text{S}_z$  phases (e.g., zinc blende for  $\text{Cu}_2\text{SnS}_3$  and cubic spinel for  $\text{Cu}_2\text{Sn}_3\text{S}_7$ ).<sup>45–48</sup> The Cu–Sn–S phase diagram is however quite rich (16 different phases, 13 of them metastable),<sup>48</sup> and therefore, the range of possible compositions for the Sn-rich NCs is very wide (from  $\text{Cu}_9\text{Sn}_2\text{S}_9$  to  $\text{Cu}_2\text{Sn}_{3.75}\text{S}_8$ ). Nevertheless, it is clear that in these NCs some degree of Sn(IV) interdiffusion has taken place, inducing crystal structure and morphology changes. Considering that only a very small fraction of the NCs is observed to be Sn-rich (<5%), we can conclude that the Sn(IV) diffusion rates in the  $\text{Cu}_{2-x}\text{S}$  NCs were negligible under the conditions prevalent in our experiments. This is consistent with previous studies in which significant Sn(IV) interdiffusion in  $\text{Cu}_{2-x}\text{S}$  NCs was only observed at temperatures as high as 240 °C.<sup>47</sup> It is worth noting that studies on the nucleation and growth of multinary Cu chalcogenide compounds (such as  $\text{CuInS}_2$ ,  $\text{Cu}_2\text{SnS}_3$ , and

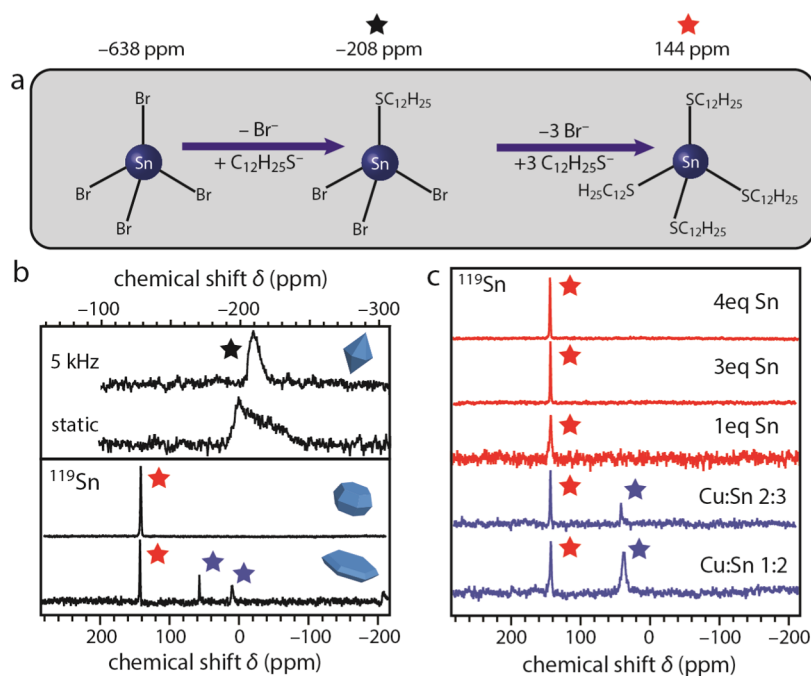


**Figure 4.** Solid-state and solution  $^{119}\text{Sn}$  NMR spectra of polyhedral  $\text{Cu}_{2-x}\text{S}$  nanocrystals and prenucleation reaction products. (a) Schematic representation of the Sn(IV)-thiolate complexes formed by stepwise replacement of bromide for deprotonated thiols. The chemical shift values for each structure are indicated at the top of the panel. (b) Solid-state  $^{119}\text{Sn}$  NMR spectra of (top panel) hexagonal  $\text{Cu}_{2-x}\text{S}$  bipyramids (with and without 5 kHz MAS) and (bottom panel) low aspect ratio  $\text{Cu}_{2-x}\text{S}$  nanoplatelets and high aspect ratio  $\text{Cu}_{2-x}\text{S}$  nanoplatelets. The symbols refer to the Sn(IV)-thiolate complexes shown in panel a. (c) Solution  $^{119}\text{Sn}$  NMR spectra of  $\text{CuCl}$  and  $\text{SnBr}_4$  mixed in the same concentration and ratio used to synthesize the nanoplatelets (blue lines) and of different equivalents of  $\text{SnBr}_4$  in DDT/OLAM (red lines).

$\text{Cu}_2\text{ZnSnS}_4$ ) have shown that binary  $\text{Cu}_2\text{S}$  NCs nucleate first, after which the other cations diffuse into the existing seeds to form the multinary NCs.<sup>6,47,49,50</sup> Therefore, we exclude separate nucleation events as a possible explanation for the observed Sn-rich NCs.

The results presented above clearly demonstrate that the impact of  $\text{SnBr}_4$  in the size and shape evolution of  $\text{Cu}_{2-x}\text{S}$  NCs synthesized by heating a solution of  $\text{CuCl}$  in DDT is due to in situ-generated Sn(IV) species and rules out Sn(IV) incorporation as the cause for the observed changes. To uncover the nature of the Sn(IV) complexes that were formed in situ and to verify whether they bind to the surface of the  $\text{Cu}_{2-x}\text{S}$  NCs, we carried out  $^1\text{H}$  and  $^{119}\text{Sn}$  NMR spectroscopic measurements.

**Solution and Solid-State NMR Spectroscopy.**  $^{119}\text{Sn}$  NMR spectroscopy is particularly suited to elucidate the nature of the Sn complexes in solution and on the surface of the NCs. Overall, the fairly high natural abundance of  $^{119}\text{Sn}$  nuclei as well as the large range of isotropic chemical shifts (around 6500 ppm) that leads to clearly separated chemical shift regions in the spectra makes  $^{119}\text{Sn}$  NMR a promising tool for characterizing tin compounds. Combined with novel NMR methods like dynamic nuclear polarization (DNP),  $^{119}\text{Sn}$  NMR also has great potential for the investigation of nanomaterial surfaces.<sup>51</sup> Furthermore, former studies have shown that the chemical shift tensor parameters of tin sulfides are highly sensitive to coordination numbers and symmetry in the local environment of the tin atom.<sup>52</sup> Therefore, probing the chemical shift anisotropy (CSA) via solid-state NMR provides an opportunity to detect structural details.

In the following, three of our  $\text{Cu}_{2-x}\text{S}$  NC morphologies were analyzed with solid-state  $^{119}\text{Sn}$  NMR, namely, the hexagonal bipyramids ( $\text{Cu}:\text{Sn} = 2:1$ ), the low aspect ratio nanoplatelets ( $\text{Cu}:\text{Sn} = 2:3$ ), and the high aspect ratio nanoplatelets ( $\text{Cu}:\text{Sn}$

$= 1:2$ ). The reference for solid-state  $^{119}\text{Sn}$  NMR measurements was  $\text{SnBr}_4$  with a sharp peak at chemical shift  $\delta -638$  ppm. None of the measured NC samples showed a detectable amount of  $\text{SnBr}_4$  in the spectra. Instead, in the cases of an excess of Sn compared to Cu, the spectra were dominated by a sharp signal at 144 ppm under static conditions as well as magic angle spinning (MAS) at 5 kHz (black lines in Figure 4b, signal at 144 ppm indicated with a red star; see also Figure S7). The fact that there is no line narrowing after spinning at 5 kHz indicates that these compounds have a symmetrical surrounding, meaning they are not on the NC surface.<sup>52</sup> Additionally, less intense and broader signals in the chemical shift ranging between 0 and 80 ppm were observed for the high aspect ratio  $\text{Cu}_{2-x}\text{S}$  nanoplatelets obtained by mixing Cu(I) and Sn(IV) salts in a 1:2 ratio (Figure 4b, indicated with blue stars). In the presence of a higher Cu amount compared to that of Sn ( $\text{Cu}:\text{Sn} = 2:1$ , bipyramids), one broad peak centered at  $-208$  ppm was detected (top of Figure 4b, indicated with a black star; see also Figure S7c). Here, 5 kHz spinning resulted in significant line narrowing (top of Figure 4b), indicating an asymmetrical surrounding. This signal was therefore assigned to a Sn compound bound to the NC surface. Comparison with the chemical shift values reported by Kovalenko et al.<sup>53,54</sup> for Sn sulfocomplexes ( $[\text{Sn}_2\text{S}_6]^{4-}$  and  $[\text{SnS}_4]^{4-}$  at  $\delta 56.3$  and  $70\text{--}75$  ppm, respectively) lead to the conclusion that the Sn(IV) species formed in situ in our experiments are of a different nature. This is further supported by the fact that the anisotropic line broadening (around 60 ppm, top of Figure 4b) of the  $^{119}\text{Sn}$  NMR spectrum obtained for hexagonal bipyramids ( $\text{Cu}:\text{Sn}$  of 2:1) is far less pronounced than reported in the literature for salts containing  $[\text{Sn}_2\text{Sn}_6]^{4-}$  ions.<sup>55</sup>

We thus propose a mechanism where thiol molecules replace bromides from  $\text{SnBr}_4$  to form Sn-thiolate complexes. This

replacement is a stepwise process, where one Br is replaced by a thiol in each step (Figure 4a). Tin(IV) methylthiolate,  $(\text{MeS})_4\text{Sn}$ , is known to show a sharp signal at 160 ppm.<sup>56,57</sup> A shift to slightly lower ppm values is expected if the methylthiolate groups are replaced by thiolate groups containing longer alkyl chains,<sup>56,57</sup> such as dodecylthiolate in the present work. The sharp signal at 144 ppm is thus assigned to  $(\text{C}_{12}\text{H}_{25}\text{S})_4\text{Sn}$  (indicated by a red star in panel a). This interpretation is supported by earlier findings, which showed that related sharp signals with a lack of prominent sidebands under slow spinning speeds (around 3 kHz) and low magnetic fields correspond to salts containing  $[\text{SnS}_4]^{4-}$  compounds.<sup>52</sup> The clear contribution of anisotropic chemical shielding (CSA) interactions to the broad signal at  $-208$  ppm indicates a nonisotropic environment of the central tin atom (Figure 4a, indicated by a black star). The lower ppm value compared to the sharp peak at 144 ppm suggests the presence of remaining Br atoms because the quadrupolar nature of  $^{79}\text{Br}$  and  $^{81}\text{Br}$  would further contribute to the line broadening. Previous studies have shown that successive replacement of Br via alkyls in tin compounds leads to a large, nonlinear shift toward higher ppm values (e.g.,  $\text{MeSnBr}_3$ ,  $-165$  ppm;  $\text{Me}_2\text{SnBr}_2$ ,  $70$  ppm;  $\text{Me}_3\text{SnBr}$ ,  $128$  ppm).<sup>54</sup> Bearing these values in mind, we attribute the signal at  $-208$  ppm to the intermediate compound  $(\text{C}_{12}\text{H}_{25}\text{S})_3\text{SnBr}$ .

Further,  $^{119}\text{Sn}$  NMR was also used to analyze the compounds present in solution prior to the onset of  $\text{Cu}_{2-x}\text{S}$  NC nucleation (Figure 4c). To this end,  $\text{CuCl}$  and  $\text{SnBr}_4$  were mixed in different Cu:Sn ratios (2:1 for hexagonal bipyramids, 2:3 for low aspect ratio nanoplatelets, and 1:2 for high aspect ratio hexagonal nanoplatelets, blue lines in Figure 4c; see also Figure S7) in a DDT/OLAM solution and heated to  $180$  °C. This temperature is slightly below the onset of  $\text{Cu}_{2-x}\text{S}$  NC nucleation ( $\sim 220$  °C as evidenced by a color change from yellow to brown), which gives rise to the formation of all precursors without (significant) formation of  $\text{Cu}_{2-x}\text{S}$  nuclei. The dominating peak at 144 ppm is present in solution as well (blue lines in Figure 4c), and a second Sn complex is observed around 80 ppm (indicated with a blue star). Furthermore, solution samples without  $\text{Cu}^+$  ions (red lines in Figure 4c; see also Figure S7) show the same signal at 144 ppm (indicated with a red star). This finding demonstrates that the formation of the compound responsible for the peak at 144 ppm is independent of the presence of  $\text{Cu}^+$  or NCs, so this peak can be unambiguously ascribed to unbound  $(\text{C}_{12}\text{H}_{25}\text{S})_4\text{Sn}$ . However, additional peaks in the range of 80–0 ppm show a clear dependency on the presence of  $\text{Cu}^+$  (peaks indicated with a blue star; only observed when Cu(I) and Sn(IV) are simultaneously present). This suggests that a thiolate complex containing both Sn(IV) and Cu(I) is present prior to the onset of  $\text{Cu}_{2-x}\text{S}$  nucleation. Heterometallic polynuclear Sn(IV)–Cu(I) complexes in which thiolates act as ligands are known to be stable both in solution and as crystalline solids.<sup>58,59</sup> It is thus plausible that similar complexes are also formed during the heating of the reaction medium to the reaction temperature. Although the chemical shift values are slightly different, the signals observed in the prenucleation solutions at 80 ppm and in the solid-state samples of high aspect ratio nanoplatelets (Cu:Sn ratio = 1:2) at 80–0 ppm might have the same origin. Different packing in the solid state and different coordination modes in solution could be a possible explanation for the differences, as has already been reported for other tin(IV) compounds.<sup>60</sup>

For further investigation, we performed  $^1\text{H}$  NMR measurements on the solution and solid-state samples (Figures S8 and S9). All three spectra for solution samples show huge proton densities at chemical shift areas characteristic for alkyl chains (3.5–0 ppm) and a peak at around 5 ppm, which typically corresponds to an  $\text{R-NH}_3^+$  species (Figure S8). This implies that the amine group of OLAM deprotonates the thiol headgroup of DDT, resulting in nucleophiles  $(\text{C}_{12}\text{H}_{25}\text{S}^-)$  that are more reactive toward both Sn(IV) and Cu(I). This is consistent with our experimental observation that the presence of OLAM increases the reaction rates. Furthermore, a peak is observed around 7.5–8 ppm, which can be ascribed to the presence of Sn(IV) because it is absent in the case of the Cu-DDT/OLAM solution (i.e., when no Sn(IV) compound is present in the reaction medium).

Copper sulfide NCs prepared with thiols as sulfur source are known to be resistant to ligand exchange procedures.<sup>61</sup> A recent study by Turo and Macdonald<sup>61</sup> provided strong evidence that, when thiols are used as sulfur source, they are effectively integrated in the NC (“crystal-bound” thiols), forming the terminal sulfur layers of the crystal and occupying high coordination number sites. These strongly bound thiols explain why ligand exchange is difficult. It is interesting to note that oleylamine capped  $\text{Cu}_{2-x}\text{S}$  NCs can only be obtained in the absence of DDT (i.e., using sulfur powder as S-source and OLAM as ligand).<sup>61</sup> Furthermore, OLAM is easily exchanged by DDT through postsynthetic ligand exchange.<sup>61</sup> The higher affinity of thiols for surface  $\text{Cu}^+$  ions can be understood considering that they have similar chemical hardness (both soft with  $\eta \approx 6$  eV),<sup>44</sup> whereas amines are harder Lewis bases than thiols. Nevertheless, amines have been shown to strongly bind to the surface of multinary Cu chalcogenide NCs, such as  $\text{CuInS}_2$  and  $\text{Cu}_2\text{ZnSnS}_4$  NCs,<sup>61–63</sup> probably because these materials contain harder Lewis acids ( $\text{In}^{3+}$ ,  $\text{Zn}^{2+}$ ,  $\text{Sn}^{4+}$ ). In these works, surface-bound amines are characterized by broad signals in the  $^1\text{H}$  NMR spectra. Our solid-state and solution  $^1\text{H}$  NMR spectra (Figures S8 and S9) provide no evidence for surface-bound amines because the only broad signal observed corresponds to  $\text{R-NH}_3^+$  species around 5 ppm. Broadening of thiol signals are hard to assign due to the high proton density corresponding to free thiol molecules, which give rise to signals at comparable chemical shifts. This makes it difficult to discriminate between free, surface-bound, and crystal-bound DDT.<sup>61</sup> Nevertheless, considering the evidence provided in ref 61, we assume that the surface of the polyhedral  $\text{Cu}_{2-x}\text{S}$  NCs prepared in the present work is capped by DDT (possibly crystal bound), whereas the amines have the adjuvant role of deprotonating the thiol headgroup (as discussed above).

**Mechanism.** On the basis of the findings discussed above, we propose a mechanism for the impact of  $\text{SnBr}_4$  and other Sn(IV) salts (e.g.,  $\text{Sn}(\text{OAc})_4$ ,  $\text{SnCl}_4$ ,  $\text{Sn}(\text{acetylacetonate})\text{Cl}_2$ ) on the size, shape, and crystal structure evolution of  $\text{Cu}_{2-x}\text{S}$  NCs formed by heating Cu salts in DDT. First, the thiolate complexes of both Cu(I) and Sn(IV) ( $\text{Cu}(\text{DDT})$  and  $\text{Sn}(\text{DDT})_4$ , respectively) are formed by replacement of the native anions by DDT. This reaction is facilitated by amines (OLAM in the present case), which deprotonate the thiol, forming a nucleophile that is sufficiently reactive to displace the native anions bound to Sn(IV). Our results (see NMR Spectroscopy section above) show that the replacement of Br by DDT occurs in a stepwise fashion, one Br at a time, until the fully substituted  $(\text{C}_{12}\text{H}_{25}\text{S})_4\text{Sn}$  complex is formed. The stability of Cu(I)–DDT is known to be higher than that of Cu(II)–

DDT,<sup>64</sup> and therefore, when Cu(II) salts are used, the formation of the Cu–DDT complex is preceded by the reduction of Cu(II) to Cu(I) by oxidation of DDT to didodecyl disulfide.<sup>41</sup>

Copper(I) thiolates are very useful as single-source precursors for the synthesis of  $\text{Cu}_{2-x}\text{S}$  NCs and have been extensively used for that purpose, both in solventless- and solution-based routes using either hot-injection or heating protocols.<sup>6,26,29,38,40,41,43,65,66</sup> The rate limiting step in the formation of  $\text{Cu}_{2-x}\text{S}$  NCs from Cu(I)–thiolates has been shown to be the thermally induced cleavage of the C–S bond,<sup>40</sup> which is catalyzed by the Cu(I) atoms<sup>87</sup> so that only DDT molecules directly bound to Cu undergo thermolysis. For [Cu–S] monomers to be formed, several C–S bonds must be cleaved because each Cu atom is coordinated to four DDT molecules.<sup>64</sup> It is interesting to note that the observations discussed above imply that the reaction temperature used in our study (225 °C) is sufficiently high to lead to thermolysis of Cu–thiolate, followed by nucleation and growth of  $\text{Cu}_{2-x}\text{S}$  NCs, but is too low to induce significant thermolysis of the C–S bonds of the Sn(IV) thiolate complexes because  $[\text{Sn}_x\text{S}_y]^{4-}$  species are not observed. Instead, our study demonstrates that the active species are  $\text{Sn}(\text{DDT})_4$  and/or the partially substituted complexes, such as  $\text{Sn}(\text{DDT})\text{Br}_3$ . The high thermal stability of  $\text{Sn}(\text{DDT})_4$  is in line with the high decomposition temperatures reported for tin(IV) thiolates and dithiocarbamates, which require temperatures ranging from 250 to 375 °C to yield  $\text{SnS}_2$ .<sup>68</sup>

To understand how the  $\text{Sn}(\text{DDT})_x\text{Br}_y$  ( $x = 1-4$ ;  $y = 0-3$ ) complexes generated in situ affect the size and shape evolution of the  $\text{Cu}_{2-x}\text{S}$  NCs, we have to consider the formation mechanism of colloidal  $\text{Cu}_{2-x}\text{S}$  NCs upon heating of a solution of CuCl in excess DDT. As discussed above, Cu–DDT is initially formed, which is followed at sufficiently high temperatures by thermolysis of the C–S bonds of the Cu–DDT complex, thereby forming [Cu–S] monomers. As a result of the high activation energies associated with the C–S bond cleavage, the precursor to monomer formation becomes the rate-limiting step in the formation of  $\text{Cu}_{2-x}\text{S}$  NCs from Cu–DDT.<sup>6,40</sup> This is in line with the general mechanism proposed for the formation of colloidal NCs of several metal chalcogenides (e.g., CdSe, PbSe, PbS)<sup>1,69-71</sup> and implies that tuning the precursor conversion kinetics can dramatically affect the nucleation and growth rates, allowing the size, shape, and crystal structure of the nanocrystals to be controlled. This size control strategy has been recently illustrated by Owen and co-workers,<sup>72</sup> who used the reactivity of substituted thiourea precursors to tune the size of NCs of a number of metal sulfides, including  $\text{Cu}_{2-x}\text{S}$ . The authors demonstrated that increasing the thiourea reactivity produces a higher concentration of smaller NCs as a result of faster monomer formation rates and, consequently, faster nucleation rates.

We propose that the dramatic impact of the  $\text{Sn}(\text{DDT})_x\text{Br}_y$  complexes on the formation of  $\text{Cu}_{2-x}\text{S}$  NCs is also due to changes in the nucleation rates. However, in contrast to the examples discussed above, in the present case the nucleation is directly affected by the  $\text{Sn}(\text{DDT})_x\text{Br}_y$  complexes, which increase the activation energy for nucleation, thereby making it more difficult (Figure 5a). This additional nucleation barrier is imposed by the interaction between the  $\text{Sn}(\text{DDT})_x\text{Br}_y$  complexes and the [Cu–S] monomers, which transiently form heterometallic polynuclear Sn(IV)–Cu(I) thiolate complexes, as observed in the NMR measurements discussed above.

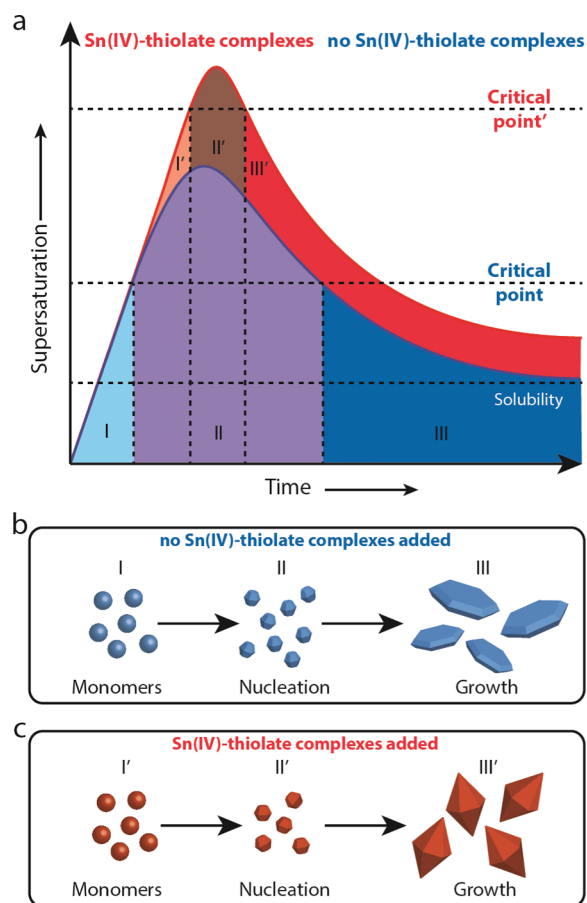


**Figure 5.** Tuning the nucleation and growth rates of  $\text{Cu}_{2-x}\text{S}$  NCs by Sn–thiolate complexes. (a) La Mer plots of nucleation and growth of  $\text{Cu}_{2-x}\text{S}$  nanocrystals (NCs) without (blue) and with Sn(IV) additives (red). The addition of Sn(IV)–thiolate complexes to  $\text{Cu}_{2-x}\text{S}$  NC synthesis results in an increase in the nucleation barrier without affecting the monomer formation rates. As a result, nucleation and growth are well separated, resulting in polyhedral NCs with narrow size and shape distributions. (b,c) Schematic representations of the two  $\text{Cu}_{2-x}\text{S}$  formation mechanisms: (b) without Sn additives, polydisperse  $\text{Cu}_{2-x}\text{S}$  nanoplatforms are obtained, and (c) with Sn additives, well-defined polyhedral  $\text{Cu}_{2-x}\text{S}$  NCs are formed.

This also implies that the higher the concentration of  $\text{Sn}(\text{DDT})_x\text{Br}_y$  complexes, the higher the nucleation barrier (Figure 5a). The monomer formation rates are not affected because they depend only on the thermolysis rates of the C–S bonds of the Cu–thiolate complexes. As a result, nucleation becomes the rate-limiting step, which impacts both the size and shape of the product  $\text{Cu}_{2-x}\text{S}$  NCs.

In the absence of  $\text{Sn}(\text{DDT})_x\text{Br}_y$  complexes, the activation energy for nucleation is low, but the monomer supply is limited by the C–S thermolysis rates. The polydisperse ensemble of relatively large nanoplatforms obtained in the absence of  $\text{SnBr}_4$  (Figure 1a) suggests that the heating rates employed in our experiments are not sufficiently fast to induce a sudden burst of C–S thermolysis and monomer formation, thereby resulting in relatively few nucleation events spread over a wide temperature range. The addition of a small concentration of  $\text{SnBr}_4$  (which is converted in situ to  $\text{Sn}(\text{DDT})_x\text{Br}_y$  complexes) already significantly increases the activation energy for nucleation, delaying it until sufficiently high temperatures have been reached. The concentration of monomers produced by

thermolysis of the Cu–DDT complexes will then be high, and a burst of nucleation followed by fast growth and depletion of the monomers becomes possible, leading to a high concentration of relatively small and monodisperse NCs (Figure 1b, 17 nm hexagonal bifrustums). Further increase in the concentration of added SnBr<sub>4</sub> leads to a higher concentration of in situ-generated Sn(DDT)<sub>x</sub>Br<sub>y</sub> complexes, which make the nucleation rates increasingly lower while keeping the monomer formation rates unaffected. As a result, the size of the product Cu<sub>2–x</sub>S NCs increases with increasing Sn(DDT)<sub>x</sub>Br<sub>y</sub> (Figure 1) because fewer nuclei are formed under a constant monomer supply (Figure 5b,c). This also affects the morphology of the NCs because facet development during growth and the final shape adopted by a colloidal NC are dictated by a balance between several driving forces,<sup>1</sup> as will be discussed below.

The growth rate of a given NC facet depends on its free energy and on the total concentration of monomers available for growth.<sup>1</sup> At low monomer activities, the overall growth rates are slow, and therefore, the differences between different crystallographic facets are not significant (thermodynamically controlled growth regime).<sup>1</sup> Consequently, the NC will grow toward an equilibrium shape that minimizes its total free energy the most, which implies that a relatively isotropic shape exposing low free-energy facets will be favored. In contrast, at high monomer activities, the overall growth rates become fast, allowing the high free-energy facets to grow faster than the low free-energy ones, outcompeting them for the monomer supply. This leads to anisotropic morphologies (kinetically controlled growth regime).<sup>1</sup> Surfactants (ligands) modify the free energy of specific facets through preferential binding, thereby depressing their growth rates relative to the facets that are less densely capped. This affects the shape evolution under both growth regimes.

Colloidal Cu<sub>2–x</sub>S NCs synthesized by thermolysis of Cu–DDT complexes have been shown to adopt a nearly spherical morphology at early growth stages or under slow growth conditions (i.e., under thermodynamic control) and a hexagonal nanoplatelet morphology under fast growth conditions (i.e., high concentrations and/or high temperatures).<sup>6,26,29,38,40,41,43,65,66</sup> This implies that the free energies of the facets in the [010] and [001] directions (namely, {101} and {221} for djurleite) are higher than that of the {100} facet. The different shapes of the Cu<sub>2–x</sub>S NCs obtained in the presence of different concentrations of SnBr<sub>4</sub> can thus be understood as a direct consequence of the impact of the in situ-generated Sn(DDT)<sub>x</sub>Br<sub>y</sub> complexes on the nucleation rates. As discussed above, the nucleation rates decrease with increasing concentration of Sn(DDT)<sub>x</sub>Br<sub>y</sub> complexes, which leads to an increasingly higher concentration of monomers available for growth, thereby enhancing the growth rates and favoring the formation of nanoplatelets with increasingly larger aspect ratios. The observation of a polydisperse ensemble of nanoplatelets in the absence of SnBr<sub>4</sub> (Figure 1a) can be ascribed to a combination of slow nucleation rates (limited by the monomer formation rates) spread over a wide temperature range and fast growth rates. The difference in the crystal structures of the differently shaped polyhedral Cu<sub>2–x</sub>S NCs (see above) can also be rationalized from this perspective, which implies that the low-chalcocite structure is thermodynamically favored, whereas the djurleite structure is kinetically favored. This is consistent with the fact that low-chalcocite is the thermodynamically stable crystal structure of Cu<sub>2</sub>S below 105 °C.<sup>42</sup>

Tin(IV) compounds (namely, Sn(acetylacetonate)Cl<sub>2</sub> and SnCl<sub>4</sub>) have been previously reported to affect the shape of Cu<sub>2–x</sub>S NCs obtained by heating Cu(II)acetylacetonate in DDT, leading to the formation of either nanosheets or nanodisks under conditions that would otherwise yield spherical NCs.<sup>73–75</sup> This effect has been tentatively ascribed to in situ-generated [Sn<sub>x</sub>S<sub>y</sub>] species that were presumed to act as selective surfactants, thereby influencing the relative growth rates of different facets and thus altering the NC morphology.<sup>73–75</sup> No evidence was provided, however, for the presence of such species, either in the reaction medium or at the surface of the product Cu<sub>2–x</sub>S NCs. It is possible that the Sn(DDT)<sub>x</sub>Br<sub>y</sub> complexes may also act as surfactants, but the NMR spectroscopy and elemental mapping results discussed above do not provide any evidence supporting to the notion that the formation of nanoplatelets is induced by selective binding of these complexes to the top and bottom facets because Sn was detected at very low concentrations and randomly distributed, regardless of the NC shape, and no Sn compounds were observed bound to the surface of the nanoplatelets. Surface-bound Sn(DDT)Br<sub>3</sub> complexes were observed, however, in the solid-state <sup>119</sup>Sn NMR spectra of the bipyramid-shaped Cu<sub>2</sub>S NCs. This suggests that Sn(DDT)<sub>x</sub>Br<sub>y</sub> complexes preferentially bind to the {302}/{502} and {364} facets, possibly because these facets have a higher free-energy and are less densely capped with DDT molecules than the top and bottom {102} facets. This adsorption is not strong enough, however, to significantly depress the growth rates of the {302}/{502} and {364} facets, but slows it sufficiently with respect to the {102} facets to allow for the formation of bipyramid NCs, which require growth both in the [100] direction and in the [010] and [001] directions. This mild down-modulation of the {302}/{502} and {364} growth is nevertheless insufficient to counteract the dramatic increase in the growth rates brought about by further increasing the concentration of the Sn(DDT)<sub>x</sub>Br<sub>y</sub> complexes because this results in lower concentration of nuclei and a large increase in the monomer concentration available for growth.

## CONCLUSIONS

We have shown that in situ-formed Sn(IV)–thiolate complexes can be used as shape-directing agents that modulate the nucleation and growth rates of polyhedral Cu<sub>2–x</sub>S NCs. Several anisotropic polyhedral NCs were obtained with narrow size and shape distributions (e.g., hexagonal bifrustums and bipyramids and hexagonal nanoplatelets with various aspect ratios) by solely changing the concentration of the additive SnBr<sub>4</sub>, which is converted in situ to Sn(IV)–thiolate complexes through a stepwise replacement of bromide by deprotonated thiols. The crystal structure of the product Cu<sub>2–x</sub>S NCs is observed to depend on the concentration of Sn(IV)–thiolate complexes, resulting in monoclinic low-chalcocite and monoclinic djurleite in the low- and high-concentration limits, respectively. Our results rule out that the impact of the Sn(IV)–thiolate complexes on the formation of Cu<sub>2–x</sub>S NCs is due to Sn incorporation in the growing NCs or to a surfactant effect. Instead, the Sn(IV)–thiolate complexes increase the Cu<sub>2–x</sub>S nucleation barrier without affecting the precursor conversion rates. This influences both the nucleation and growth rates and leads to a better separation between nucleation and growth, thereby decreasing the ensemble polydispersity. It also dictates the final shape and structure of the product Cu<sub>2–x</sub>S NCs by affecting the balance between the nucleation and growth rates



under constant monomer formation rates. In the low-concentration limit, the nucleation rates are relatively fast, leading to a high concentration of nuclei and a low concentration of monomers available for growth. This results in slow growth under thermodynamic control. The nucleation rates decrease with increasing concentration of Sn(IV)–thiolate complexes, which leaves an increasingly higher concentration of monomers available for growth. This progressively enhances the growth rates, thereby shifting the growth to the kinetically controlled regime.

The use of inorganic ligands as shape-directing agents has not been extensively studied yet and could possibly lead to novel NC morphologies and improved size control strategies. This could be beneficial for implementation of NCs in, for example, photovoltaic and photonic devices for which well-defined building blocks are required to form highly ordered thin layers of individual NCs. In combination with topotactic cation exchange reactions, this could boost the importance of the synthetic strategy developed in this work, giving rise to tailor-made NCs and NC solids with novel functionalities, which may prove beneficial for a number of applications.

## ■ ASSOCIATED CONTENT

### Supporting Information

The Supporting Information is available free of charge on the ACS Publications website at DOI: [10.1021/acs.chemmater.6b03098](https://doi.org/10.1021/acs.chemmater.6b03098).

PED patterns, X-ray diffractograms, HRTEM, TEM, HAADF-STEM, EDS, and dark-field STEM images, and  $^{119}\text{Sn}$  and  $^1\text{H}$  NMR spectra (PDF)

## ■ AUTHOR INFORMATION

### Corresponding Author

\*E-mail: [c.demello-donega@uu.nl](mailto:c.demello-donega@uu.nl).

### Notes

The authors declare no competing financial interest.

## ■ ACKNOWLEDGMENTS

W.v.d.S. and C.d.M.D. acknowledge financial support from the division of Chemical Sciences (CW) of The Netherlands Organization for Scientific Research (NWO) under grant number ECHO.712.012.001. M.B. also gratefully acknowledges NWO for funding the NMR infrastructure (Middle Groot program, grant number 700.58.102). S.B. acknowledges financial support from the European Research Council (ERC Starting Grant # 335078-COLOURATOMS).

## ■ REFERENCES

- (1) Donega, C. d. M. Synthesis and Properties of Colloidal Heteronanocrystals. *Chem. Soc. Rev.* **2011**, *40*, 1512–1546.
- (2) Kovalenko, M. V.; Manna, L.; Cabot, A.; Hens, Z.; Talapin, D. V.; Kagan, C. R.; Klimov, V. I.; Rogach, A. L.; Reiss, P.; Milliron, D. J.; et al. Prospects of Nanoscience with Nanocrystals. *ACS Nano* **2015**, *9*, 1012–1057.
- (3) Talapin, D. V.; Lee, J. S.; Kovalenko, M. V.; Shevchenko, E. V. Prospects of Colloidal Nanocrystals for Electronic and Optoelectronic Applications. *Chem. Rev.* **2010**, *110*, 389–458.
- (4) Grim, J. Q.; Manna, L.; Moreels, I. A Sustainable Future for Photonic Colloidal Nanocrystals. *Chem. Soc. Rev.* **2015**, *44*, 5897–5914.
- (5) Shirasaki, Y.; Supran, G.; Bawendi, M.; Bulović, V. Emergence of Colloidal Quantum-Dot Light-Emitting Technologies. *Nat. Photonics* **2012**, *7*, 13–23.

- (6) van der Stam, W.; Berends, A. C.; de Mello Donega, C. Prospects of Colloidal Copper Chalcogenide Nanocrystals. *ChemPhysChem* **2016**, *17*, 559–581.

- (7) Zhang, Y.; Xie, C.; Su, H.; Liu, J.; Pickering, S.; Wang, Y.; Yu, W. W.; Wang, J.; Wang, Y.; Hahn, J.; et al. Employing Heavy Metal-Free Colloidal Quantum Dots in Solution-Processed White Light-Emitting Diodes. *Nano Lett.* **2011**, *11*, 329–332.

- (8) Kolny-Olesiak, J.; Weller, H. Synthesis and Application of Colloidal CuInS<sub>2</sub> Semiconductor Nanocrystals. *ACS Appl. Mater. Interfaces* **2013**, *5*, 12221–12237.

- (9) Luther, J. M.; Jain, P. K.; Ewers, T.; Alivisatos, A. P. Localized Surface Plasmon Resonances Arising from Free Carriers in Doped Quantum Dots. *Nat. Mater.* **2011**, *10*, 361–366.

- (10) Burda, C.; Chen, X.; Narayanan, R.; El-Sayed, M. A. Chemistry and Properties of Nanocrystals of Different Shapes. *Chem. Rev.* **2005**, *105*, 1025–1102.

- (11) Zhao, Y.; Pan, H.; Lou, Y.; Qiu, X.; Zhu, J.; Burda, C. Plasmonic Cu<sub>2-x</sub>S Nanocrystals: Optical and Structural Properties of Copper-Deficient Copper(I) Sulfides. *J. Am. Chem. Soc.* **2009**, *131*, 4253–4261.

- (12) Zhuang, Z.; Peng, Q.; Zhang, B.; Li, Y. Controllable Synthesis of Cu<sub>2</sub>S Nanocrystals and Their Assembly into a Superlattice. *J. Am. Chem. Soc.* **2008**, *130*, 10482–10483.

- (13) Xie, Y.; Riedinger, A.; Prato, M.; Casu, A.; Genovese, A.; Guardia, P.; Sottini, S.; Sangregorio, C.; Miszta, K.; Ghosh, S.; et al. Copper Sulfide Nanocrystals with Tunable Composition by Reduction of Covellite Nanocrystals with Cu<sup>+</sup> Ions. *J. Am. Chem. Soc.* **2013**, *135*, 17630–17637.

- (14) Page, M.; Niiitsoo, O.; Itzhaik, Y.; Cahen, D.; Hodes, G. Copper Sulfide as a Light Absorber in Wet-Chemical Synthesized Extremely Thin Absorber (ETA) Solar Cells. *Energy Environ. Sci.* **2009**, *2*, 220–223.

- (15) Wu, Y.; Wadia, C.; Ma, W.; Sadler, B.; Alivisatos, A. P. Synthesis and Photovoltaic Application of Copper (I) Sulfide Nanocrystals. *Nano Lett.* **2008**, *8*, 2551–2555.

- (16) Xie, Y.; Carbone, L.; Nobile, C.; Grillo, V.; D'Agostino, S.; Della Sala, F.; Giannini, C.; Altamura, D.; Oelsner, C.; Krysch, C.; et al. Metallic-like Stoichiometric Copper Sulfide Nanocrystals: Phase- and Shape-Selective Synthesis, Near-Infrared Surface Plasmon Resonance Properties, and Their Modeling. *ACS Nano* **2013**, *7*, 7352–7369.

- (17) Kriegel, I.; Rodríguez-Fernández, J.; Wisnet, A.; Zhang, H.; Waurisch, C.; Eychmüller, A.; Dubavik, A.; Govorov, A. O.; Feldmann, J. Shedding Light on Vacancy-Doped Copper Chalcogenides: Shape-Controlled Synthesis, Optical Properties, and Modeling of Copper Telluride Nanocrystals with near-Infrared Plasmon Resonances. *ACS Nano* **2013**, *7*, 4367–4377.

- (18) Dorfs, D.; Härtling, T.; Miszta, K.; Bigall, N. C.; Kim, M. R.; Genovese, A.; Falqui, A.; Povia, M.; Manna, L. Reversible Tunability of the Near-Infrared Valence Band Plasmon Resonance in Cu<sub>2-x</sub>Se Nanocrystals. *J. Am. Chem. Soc.* **2011**, *133*, 11175–11180.

- (19) Liu, Y.; Deng, Y.; Sun, Z.; Wei, J.; Zheng, G.; Asiri, A. M.; Khan, S. B.; Rahman, M. M.; Zhao, D. Hierarchical Cu<sub>2</sub>S Microsponges Constructed from Nanosheets for Efficient Photocatalysis. *Small* **2013**, *9*, 2702–2708.

- (20) Vinokurov, K.; Elimelech, O.; Millo, O.; Banin, U. Copper Sulfide Nanocrystals Level Structure and Electrochemical Functionality towards Sensing Applications. *ChemPhysChem* **2016**, *17*, 675–680.

- (21) Hsu, S.; Bryks, W.; Tao, A. R. Effects of Carrier Density and Shape on the Localized Surface Plasmon Resonances of Cu<sub>2-x</sub>S Nanodisks. *Chem. Mater.* **2012**, *24*, 3765–3771.

- (22) Wolf, A.; Härtling, T.; Hinrichs, D.; Dorfs, D. Synthesis of Plasmonic Cu<sub>2-x</sub>Se@ZnS Core@Shell Nanoparticles. *ChemPhysChem* **2016**, *17*, 717–723.

- (23) van der Stam, W.; Rabouw, F. T.; Vonk, S. J. W.; Geuchies, J. J.; Ligthart, H.; Petukhov, A. V.; de Mello Donega, C. Oleic Acid-Induced Atomic Alignment of ZnS Polyhedral Nanocrystals. *Nano Lett.* **2016**, *16*, 2608–2614.

- (24) Reifsnnyder, D. C.; Ye, X.; Gordon, T. R.; Song, C.; Murray, C. B. Three-Dimensional Self-Assembly of Chalcopyrite Copper Indium Diselenide Nanocrystals into Oriented Films. *ACS Nano* **2013**, *7*, 4307–4315.
- (25) van der Stam, W.; Gantapara, A. P.; Akkerman, Q. A.; Soligno, G.; Meeldijk, J. D.; van Roij, R.; Dijkstra, M.; de Mello Donega, C. Self-Assembly of Colloidal Hexagonal Bipyramid- and Bifrustum-Shaped ZnS Nanocrystals into Two-Dimensional Superstructures. *Nano Lett.* **2014**, *14*, 1032–1037.
- (26) Kruszynska, M.; Borchert, H.; Bachmatiuk, A.; Rummeli, M. H.; Büchner, B.; Parisi, J.; Kolny-Olesiak, J. Size and Shape Control of Colloidal Copper(I) Sulfide Nanorods. *ACS Nano* **2012**, *6*, 5889–5896.
- (27) Sigman, M.; Ghezlbash, A.; Hanrath, T.; Saunders, A. E.; Lee, F.; Korgel, B. A. Solventless Synthesis of Monodisperse Cu<sub>2</sub>S Nanorods, Nanodisks, and Nanoplatelets. *J. Am. Chem. Soc.* **2003**, *125*, 16050–16057.
- (28) Li, W.; Shavel, A.; Guzman, R.; Rubio-Garcia, J.; Flox, C.; Fan, J.; Cadavid, D.; Ibañez, M.; Arbiol, J.; Morante, J. R.; Cabot, A. Morphology Evolution of Cu<sub>2-x</sub>S Nanoparticles: From Spheres to Dodecahedrons. *Chem. Commun.* **2011**, *47*, 10332–10334.
- (29) van der Stam, W.; Akkerman, Q. A.; Ke, X.; van Huis, M. A.; Bals, S.; de Mello Donega, C. Solution-Processable Ultrathin Size- and Shape-Controlled Colloidal Cu<sub>2-x</sub>S Nanosheets. *Chem. Mater.* **2015**, *27*, 283–291.
- (30) Beberwyck, B. J.; Surendranath, Y.; Alivisatos, A. P. Cation Exchange: A Versatile Tool for Nanomaterials Synthesis. *J. Phys. Chem. C* **2013**, *117*, 19759–19770.
- (31) Gupta, S.; Kershaw, S. V.; Rogach, A. L. 25th Anniversary Article: Ion Exchange in Colloidal Nanocrystals. *Adv. Mater.* **2013**, *25*, 6923–6944.
- (32) Li, H.; Zanella, M.; Genovese, A.; Povia, M.; Falqui, A.; Giannini, C.; Manna, L. Sequential Cation Exchange in Nanocrystals: Preservation of Crystal Phase and Formation of Metastable Phases. *Nano Lett.* **2011**, *11*, 4964–4970.
- (33) van der Stam, W.; Berends, A. C.; Rabouw, F. T.; Willhammar, T.; Ke, X.; Meeldijk, J. D.; Bals, S.; de Mello Donega, C. Luminescent CuInS<sub>2</sub> Quantum Dots by Partial Cation Exchange in Cu<sub>2-x</sub>S Nanocrystals. *Chem. Mater.* **2015**, *27*, 621–628.
- (34) Ha, D.-H.; Caldwell, A. H.; Ward, M. J.; Honrao, S.; Mathew, K.; Hovden, R.; Koker, M. K. A.; Muller, D. A.; Hennig, R. G.; Robinson, R. D. Solid–Solid Phase Transformations Induced through Cation Exchange and Strain in 2D Heterostructured Copper Sulfide Nanocrystals. *Nano Lett.* **2014**, *14*, 7090–7099.
- (35) Luther, J. M.; Zheng, H.; Sadtler, B.; Alivisatos, A. P. Synthesis of PbS Nanorods and Other Ionic Nanocrystals of Complex Morphology by Sequential Cation Exchange Reactions. *J. Am. Chem. Soc.* **2009**, *131*, 16851–16857.
- (36) van der Stam, W.; Bladt, E.; Rabouw, F. T.; Bals, S.; de Mello Donega, C. Near-Infrared Emitting CuInSe<sub>2</sub>/CuInS<sub>2</sub> Dot Core/Rod Shell Heteronanorods by Sequential Cation Exchange. *ACS Nano* **2015**, *9*, 11430–11438.
- (37) de Trizio, L.; Manna, L. Forging Colloidal Nanostructures via Cation Exchange Reactions. *Chem. Rev.* **2016**, DOI: 10.1021/acs.chemrev.5b00739.
- (38) Kuzuya, T.; Tai, Y.; Yamamuro, S.; Sumiyama, K. Synthesis of Copper and Zinc Sulfide Nanocrystals via Thermolysis of the Polymetallic Thiolate Cage. *Sci. Technol. Adv. Mater.* **2005**, *6*, 84–90.
- (39) Palenstijn, W. J.; Batenburg, K. J.; Sijbers, J. Performance Improvements for Iterative Electron Tomography Reconstruction Using Graphics Processing Units (GPUs). *J. Struct. Biol.* **2011**, *176*, 250–253.
- (40) Bryks, W.; Wette, M.; Velez, N.; Hsu, S.; Tao, A. R. Supramolecular Precursors for the Synthesis of Anisotropic Cu<sub>2</sub>S Nanocrystals. *J. Am. Chem. Soc.* **2014**, *136*, 6175–6178.
- (41) Norby, P.; Johnsen, S.; Iversen, B. B. *In Situ* X-Ray Diffraction Study of the Formation, Growth, and Phase Transition of Colloidal Cu<sub>2-x</sub>S Nanocrystals. *ACS Nano* **2014**, *8*, 4295–4303.
- (42) Evans, H. Crystal Structure of Low Chalcocite. *Nature, Phys. Sci.* **1971**, *232*, 69–70.
- (43) van der Stam, W.; Rabouw, F. T.; Geuchies, J. J.; Berends, A. C.; Hinterding, S. O. M.; Geitenbeek, R. G.; van der Lit, J.; Prévost, S.; Petukhov, A. V.; de Mello Donega, C. *In Situ* Probing of Stack-Templated Growth of Ultrathin Cu<sub>2-x</sub>S Nanosheets. *Chem. Mater.* **2016**, DOI: 10.1021/acs.chemmater.6b02787.
- (44) Pearson, R. G. Absolute Electronegativity and Hardness: Application to Inorganic Chemistry. *Inorg. Chem.* **1988**, *27*, 734–740.
- (45) Chang, J.; Waclawik, E. R. Controlled Synthesis of CuInS<sub>2</sub>, Cu<sub>2</sub>SnS<sub>3</sub> and Cu<sub>2</sub>ZnSnS<sub>4</sub> Nano-Structures: Insight into the Universal Phase-Selectivity Mechanism. *CrystEngComm* **2013**, *15*, 5612–5619.
- (46) Wang, J.; Liu, P.; Seaton, C. C.; Ryan, K. M. Complete Colloidal Synthesis of Cu<sub>2</sub>SnSe<sub>3</sub> Nanocrystals with Crystal Phase and Shape Control. *J. Am. Chem. Soc.* **2014**, *136*, 7954–7960.
- (47) Tan, J. M. R.; Lee, Y. H.; Pedireddy, S.; Baikie, T.; Ling, X. Y.; Wong, L. H. Understanding the Synthetic Pathway of a Single-Phase Quaternary Semiconductor Using Surface-Enhanced Raman Scattering: A Case of Wurtzite Cu<sub>2</sub>ZnSnS<sub>4</sub> Nanoparticles. *J. Am. Chem. Soc.* **2014**, *136*, 6684–6692.
- (48) Fiechter, S.; Martinez, M.; Schmidt, G.; Henrion, W.; Tamm, Y. Phase Relations and Optical Properties of Semiconducting Ternary Sulfides in the System Cu–Sn–S. *J. Phys. Chem. Solids* **2003**, *64*, 1859–1862.
- (49) Kruszynska, M.; Parisi, J.; Kolny-Olesiak, J. Synthesis and Shape Control of Copper Tin Sulphide Nanocrystals and Formation of Gold–Copper Tin Sulphide Hybrid Nanostructures. *Z. Naturforsch., A: Phys. Sci.* **2014**, *69*, 2–6.
- (50) Kruszynska, M.; Borchert, H.; Parisi, J.; Kolny-Olesiak, J. Synthesis and Shape Control of CuInS<sub>2</sub> Nanoparticles. *J. Am. Chem. Soc.* **2010**, *132*, 15976–15986.
- (51) Protesescu, L.; Rossini, A. J.; Kriegner, D.; Valla, M.; Kergommeaux, A. de; Walter, M.; Kravchyk, K. V.; Nachttegaal, M.; Stangl, J.; Malaman, B.; et al. Unraveling the Core-Shell Structure of Ligand-Capped Sn/SnO<sub>x</sub> Nanoparticles by Surface-Enhanced Nuclear Magnetic Resonance, Mössbauer, and X-Ray Absorption Spectroscopies. *ACS Nano* **2014**, *8*, 2639–2648.
- (52) Mundus, C.; Taillades, G.; Pradel, A.; Ribes, M. A Sn Solid-State Nuclear Magnetic Resonance Study of Crystalline Tin Sulphides. *Solid State Nucl. Magn. Reson.* **1996**, *7*, 141–146.
- (53) Kovalenko, M. V.; Bodnarchuk, M. I.; Zaumseil, J.; Lee, J.-S.; Talapin, D. V. Expanding the Chemical Versatility of Colloidal Nanocrystals Capped with Molecular Metal Chalcogenide Ligands. *J. Am. Chem. Soc.* **2010**, *132*, 10085–10092.
- (54) Kovalenko, M. V.; Scheele, M.; Talapin, D. V. Colloidal Nanocrystals with Molecular Metal Chalcogenide Surface Ligands. *Science* **2009**, *324*, 1417–1420.
- (55) Rangan, K. K.; Trikalitis, P. N.; Canlas, C.; Bakas, T.; Weliky, D. P.; Kanatzidis, M. G. Hexagonal Pore Organization in Mesoporous Metal Tin Sulfides Built with [Sn<sub>2</sub>S<sub>6</sub>]<sup>4+</sup> Cluster. *Nano Lett.* **2002**, *2*, 513–517.
- (56) Gielen, M. *Tin Chemistry: Fundamentals, Frontiers and Applications*; Wiley, 2008.
- (57) Günther, H. *NMR Spectroscopy: Basic Principles, Concepts and Applications in Chemistry*; Wiley, 2013.
- (58) Wang, X.; Sheng, T.-L.; Fu, R.-B.; Hu, S.-M.; Xiang, S.-C.; Wang, L.-S.; Wu, X.-T. Assembly of a Heterometallic Polynuclear Sn(IV)-Cu(I) Cluster Based on Sn(edt)<sub>2</sub> (edt = Ethane-1,2-Dithiolate) as a Metalloligand. *Inorg. Chem.* **2006**, *45*, 5236–5238.
- (59) Wang, L.-S.; Sheng, T.-L.; Wang, X.; Chen, D.-B.; Hu, S.-M.; Fu, R.-B.; Xiang, S.-C.; Wu, X.-T. Self-Assembly of Luminescent Sn(IV)/Cu/S Clusters Using Metal Thiolates as Metalloligands. *Inorg. Chem.* **2008**, *47*, 4054–4059.
- (60) Jiao, J.; Lee, M.; Barnes, E.; Hagaman, E. W. Sn NMR Chemical Shift Tensors in Anhydrous and Hydrated Si<sub>8</sub>O<sub>20</sub>(SnMe<sub>3</sub>)<sub>8</sub> Crystals. *Magn. Reson. Chem.* **2008**, *46*, 690–692.
- (61) Turo, M. J.; Macdonald, J. E. Crystal-Bound vs Surface-Bound Thiols on Nanocrystals. *ACS Nano* **2014**, *8*, 10205–10213.

(62) Dierick, R.; Van den Broeck, F.; De Nolf, K.; Zhao, Q.; Vantomme, A.; Martins, J. C.; Hens, Z. Surface Chemistry of  $\text{CuInS}_2$  Colloidal Nanocrystals, Tight Binding of L-Type Ligands. *Chem. Mater.* **2014**, *26*, 5950–5957.

(63) Shavel, A.; Ibáñez, M.; Luo, Z.; De Roo, J.; Carrete, A.; Dimitrievska, M.; Genc, A.; Meyns, M.; Pérez-Rodríguez, A.; Kovalenko, M. V.; et al. Scalable Heating-Up Synthesis of Monodisperse  $\text{Cu}_2\text{ZnSnS}_4$  Nanocrystals. *Chem. Mater.* **2016**, *28*, 720–726.

(64) Espinet, P.; Lequerica, M. C.; Martín-Alvarez, J. M. Synthesis, Structural Characterization and Mesogenic Behavior of Copper (I) n-Alkylthiolates. *Chem. - Eur. J.* **1999**, *5*, 1982–1986.

(65) Han, W.; Yi, L.; Zhao, N.; Tang, A.; Gao, M.; Tang, Z. Synthesis and Shape-Tailoring of Copper Sulfide/Indium Sulfide-Based Nanocrystals. *J. Am. Chem. Soc.* **2008**, *130*, 13152–13161.

(66) Li, S.; Wang, H.; Xu, W.; Si, H.; Tao, X.; Lou, S.; Du, Z.; Li, L. S. Synthesis and Assembly of Monodisperse Spherical  $\text{Cu}_2\text{S}$  Nanocrystals. *J. Colloid Interface Sci.* **2009**, *330*, 483–487.

(67) Wang, L.; He, W.; Yu, Z. Transition-Metal Mediated Carbon–Sulfur Bond Activation and Transformations. *Chem. Soc. Rev.* **2013**, *42*, 599–621.

(68) Barone, G.; Chaplin, T.; Hibbert, T. G.; Kana, A. T.; Mahon, M. F.; Molloy, K. C.; Worsley, I. D.; Parkin, I. P.; Price, L. S. Synthesis and Thermal Decomposition Studies of Homo- and Heteroleptic Tin(IV) Thiolates and Dithiocarbamates: Molecular Precursors for Tin Sulfides. *J. Chem. Soc. Dalton Trans.* **2002**, *6*, 1085–1092.

(69) Owen, J. S.; Chan, E. M.; Liu, H.; Alivisatos, A. P. Precursor Conversion Kinetics and the Nucleation of Cadmium Selenide Nanocrystals. *J. Am. Chem. Soc.* **2010**, *132*, 18206–18213.

(70) Abe, S.; Čapek, R. K.; de Geyter, B.; Hens, Z. Tuning the Postfocused Size of Colloidal Nanocrystals by the Reaction Rate: From Theory to Application. *ACS Nano* **2012**, *6*, 42–53.

(71) Rempel, J. Y.; Bawendi, M. G.; Jensen, K. F. Insights into the Kinetics of Semiconductor Nanocrystal Nucleation and Growth. *J. Am. Chem. Soc.* **2009**, *131*, 4479–4489.

(72) Hendricks, M. P.; Campos, M. P.; Cleveland, G. T.; Plante, I. J.; Owen, J. S. A Tunable Library of Substituted Thiourea Precursors to Metal Sulfide Nanocrystals. *Science* **2015**, *348*, 1226–1230.

(73) Li, X.; Shen, H.; Niu, J.; Li, S.; Zhang, Y.; Wang, H.; Li, L. S. Columnar Self-Assembly of  $\text{Cu}_2\text{S}$  Hexagonal Nanoplates Induced by Tin(IV)-X Complex as Inorganic Surface Ligand. *J. Am. Chem. Soc.* **2010**, *132*, 12778–12779.

(74) Li, X.; Wang, M.; Shen, H.; Zhang, Y.; Wang, H.; Li, L. S. Inorganic Sn-X-Complex-Induced 1D, 2D, and 3D Copper Sulfide Superstructures from Anisotropic Hexagonal Nanoplate Building Blocks. *Chem. - Eur. J.* **2011**, *17*, 10357–10364.

(75) Yi, L.; Gao, M. From Ultrathin Two-Dimensional Djurleite Nanosheets to One-Dimensional Nanorods Comprised of Djurleite Nanoplates: Synthesis, Characterization, and Formation Mechanism. *Cryst. Growth Des.* **2011**, *11*, 1109–1116.